Unified View of Sediment Transport by Currents and Waves. IV: Application of Morphodynamic Model

Leo C. van Rijn[1]; Dirk-Jan R. Walstra[2]; and Maarten van Ormondt[3]

Abstract: The TR2004 transport formulations for clay, silt, and sand as proposed in Parts 1 and 2 have been implemented in morphodynamic models to predict bed level changes. These models have been verified using various laboratory and field data cases concerning coastal flow in offshore and near-shore zones. Furthermore, the model has been applied to two complicated sediment environments concerning the flow around a spurdike in a river and the tidal flow of cohesive sediments in the Yangtze Estuary in China. Overall, it is concluded that the morphodynamic models using default settings performs reasonably well. The applied scaling factors of the sediment transport model are in the generally accepted range of 0.5–2.

DOI: 10.1061/(ASCE)0733-9429(2007)133:7(776)

CE Database subject headings: Sediment; Currents; Dynamic models; Coastal morphology.

Introduction

In this Part 4 the knowledge on cohesive and noncohesive sediment transport and bed roughness as proposed and explained in Parts 1 and 2 (the TR2004 sediment transport model) is applied in a three-dimensional (3D), time-dependent hydrodynamic model (DELFT3D) (see Lesser et al. 2004) and in a two-dimensional cross-shore model (CROSMOR) (see van Rijn et al. 1999, 2003), yielding morphodynamic models for the full range of bed conditions from very fine silts (about 10 μm) to gravel (2,000 μm). The 3D model can be operated in line mode (1DH or 2DV) or in area mode (2DH or 3D), in single-layer or in multilayer mode for riverine, estuarine as well as coastal flows. Important effects such as flocculation, hindered settling, and turbulence damping are automatically introduced based on bed sediment characteristics (input) and computed sediment concentrations. The 2D CROSMOR-model can only operate along a cross-shore transect using a "wave-by-wave" approach (probabilistic) and assuming uniformity in alongshore direction. Near-shore wave effects—asymmetric shoaling waves, nonlinear effects, breaking waves, near-bed streaming and near-bed return flows, and wave- and current-related sand transport (Walstra et al. 2000; Van Rijn et al. 1999)—are included in both models (CROSMOR; DELFT3D). The transport values computed by the 3D model are compared to those of the stand-alone transport model TR2004 (see Parts 1, 2, and 3). Details of the implementation are given by van Rijn et al. (2004).

The major part of this paper focusses on the verification of the morphodynamic model to show that the simple engineering transport components (Parts 1 and 2) produce realistic morphological results ("the proof of the pudding is in the eating"). Information on the verification of the flow model is given by Lesser et al. (2004), Walstra et al. (2003), and Sutherland et al. (2004) and will not be repeated herein. Generally, three steps can be distinguished in the model verification procedure (Wang and Wu 2005). In Step 1 the model results are compared to the results of analytic solutions to evaluate whether the mathematical expressions simulating the physics of interest are solved correctly by the numerical model. This has been done successfully in earlier studies and will not be repeated herein (van Rijn 1986, 1987; Lesser et al. 2004). In Step 2 the model results are compared to small- and large-scale laboratory results, which are conducted in well controlled conditions. Using detailed laboratory data, the most fundamental physical processes of the model can be tested severely. Herein, one small-scale laboratory data set concerning coastal flow with combined current and nonbreaking wave conditions and two large-scale laboratory experiments concerning cross-shore bar behavior in the surf zone with breaking waves are used to evaluate the morphodynamic models. In Step 3 the model results are compared to real world data to evaluate the ability of the model for daily engineering practice. In this paper, two field cases concerning coastal flows with tidal velocities and nonbreaking waves (in the Dutch sector of the North Sea) are considered. Short-term (1 year) as well as long-term (14 years) cases are considered. In all runs the morphodynamic model is tested in fully predictive mode, which implies that not only the sediment transport will be predicted but also the bed roughness values in response to the sediment dynamics and hydrodynamics are predicted. The bed roughness is also used (feedback) in the flow and wave prediction models. No additional calibration is applied. Finally, two field cases with less data are considered to show the ability of the 3D model to simulate the flow, sediment transport, and associated bed level changes in complicated sediment environments concerning the steady upstream flow and scour near a large spurdike in a river, the nonsteady tidal flow of cohesive sediments in the large-scale Yangtze Estuary in China.

[1]Delft Hydraulics, P.O. Box 177, 2600 MH, Delft, The Netherlands; and, Professor, Dept. of Physical Geography, Univ. Utrecht, Utrecht, The Netherlands.

[2]Delft Hydraulics, P.O. Box 177, 2600 MH, Delft, The Netherlands.

[3]Delft Hydraulics, P.O. Box 177, 2600 MH, Delft, The Netherlands.

Note. Discussion open until December 1, 2007. Separate discussions must be submitted for individual papers. To extend the closing date by one month, a written request must be filed with the ASCE Managing Editor. The manuscript for this paper was submitted for review and possible publication on July 8, 2005; approved on August 2, 2006. This paper is part of the ***Journal of Hydraulic Engineering***, Vol. 133, No. 7, July 1, 2007. ©ASCE, ISSN 0733-9429/2007/7-776–793/$25.00.

Implementation Three-Dimensional Model

General

The 3D-FLOW module solves the unsteady shallow-water equations in one (1DH), two (2DV or 2DH), or three dimensions. The system of equations consists of the horizontal momentum equations, the continuity equation, the transport equation, and a turbulence closure model. The vertical momentum equation is reduced to the hydrostatic pressure relation as vertical accelerations are assumed to be small compared to gravitational acceleration and are not taken into account. This makes the 3D model suitable for predicting the flow in shallow seas, coastal areas, estuaries, lagoons, rivers, and lakes. The user may choose whether to solve the hydrodynamic equations on a Cartesian rectangular, orthogonal curvilinear (boundary fitted), or spherical grid. In three-dimensional simulations a boundary fitted (σ coordinate) approach as well as a fixed grid are available for the vertical grid direction. However, herein the equations are presented in their Cartesian rectangular form only using σ layers for the vertical direction. Furthermore, a detailed description of the model is outside the scope of this paper. A detailed description of the implemented wave model and hydrodynamics can be found in Lesser et al. (2004). Herein, the basic equations are presented and then the attention is focused on the implementation of the TRANSPOR2004 sediment transport formulations (see Parts 1 and 2) in the 3D model, and finally the verification of the model against laboratory and field data.

Basic Flow and Sediment Equations

The vertical σ coordinate is scaled as $(-1 \le \sigma \le 0)$

$$\sigma = \frac{z - \zeta}{h} \tag{1}$$

where z=vertical coordinate from mean surface level upwards (multilayer model; bottom at $z=-d$, surface at $z=\zeta$); $h=d+\zeta$=water depth; d=depth to mean sea level; and ζ=water level to mean sea level. The horizontal momentum equations are (Stelling and Van Kester 1994)

$$\frac{\partial U}{\partial t} + U\frac{\partial U}{\partial x} + V\frac{\partial U}{\partial y} + \frac{\omega}{h}\frac{\partial U}{\partial \sigma} - fV = -\frac{1}{\rho_0}P_x + F_x + M_x + \frac{1}{(h)^2}\frac{\partial}{\partial \sigma}\left(\nu_V \frac{\partial U}{\partial \sigma}\right)$$

$$\frac{\partial V}{\partial t} + U\frac{\partial V}{\partial x} + V\frac{\partial V}{\partial y} + \frac{\omega}{h}\frac{\partial V}{\partial \sigma} + fU = -\frac{1}{\rho_0}P_y + F_y + M_y + \frac{1}{(h)^2}\frac{\partial}{\partial \sigma}\left(\nu_V \frac{\partial V}{\partial \sigma}\right) \tag{2}$$

where U,V=fluid velocities in the x,y-directions; ρ_0=reference fluid density (fresh water density); ω=vertical fluid velocity relative to the moving σ plane; ν_V=eddy viscosity coefficient in vertical direction; and f=Coriolis coefficient. The M_x and M_y terms represent the contributions due to external sources or sinks of momentum (external forces by hydraulic structures, discharge, or withdrawal of water, wave stresses, etc.). F=external forces; P=pressure terms; and P_x and P_y, are given by (Boussinesq approximations)

$$\frac{1}{\rho_0}P_x = g\frac{\partial \zeta}{\partial x} + g\frac{h}{\rho_0}\int_\sigma^0 \left(\frac{\partial \rho}{\partial x} + \frac{\partial \sigma'}{\partial x}\frac{\partial \rho}{\partial \sigma'}\right)d\sigma'$$

$$\frac{1}{\rho_0}P_y = g\frac{\partial \zeta}{\partial y} + g\frac{h}{\rho_0}\int_\sigma^0 \left(\frac{\partial \rho}{\partial y} + \frac{\partial \sigma'}{\partial y}\frac{\partial \rho}{\partial \sigma'}\right)d\sigma' \tag{3}$$

The horizontal Reynold's stresses, F_x and F_y, are determined using the eddy viscosity concept, which for large-scale simulations reduces to

$$F_x = \nu_H\left(\frac{\partial^2 U}{\partial x^2} + \frac{\partial^2 U}{\partial y^2}\right)$$

$$F_y = \nu_H\left(\frac{\partial^2 V}{\partial x^2} + \frac{\partial^2 V}{\partial y^2}\right) \tag{4}$$

in which the gradients are taken along σ planes. Various turbulence models are available to determine the vertical eddy viscosity values (ν_v). The horizontal diffusivity values (ν_H) can be specified as a scalar or computed by a subgrid model (HLES model). The depth-averaged continuity equation is given by

$$\frac{\partial \zeta}{\partial t} + \frac{\partial [h\bar{U}]}{\partial x} + \frac{\partial [h\bar{V}]}{\partial y} = S \tag{5}$$

where $\bar{U},\bar{V}$=depth-mean velocities; and S=contributions per unit area due to the discharge or withdrawal of water, evaporation, and precipitation. The vertical flow velocity ω in z direction is derived from the 3D continuity (mass balance) equation for the fluid.

Surface-Wave Effects

Wave effects can also be included in 3D-FLOW simulations by running the separate 3D-WAVE module. A call to the 3D-WAVE module must be made prior to the running of the FLOW module. The results are stored on a communication file on the same computational grid as used by the FLOW module. The FLOW module can then read the wave results and include them in flow calculations. Wave simulations may be performed using the second-generation wave model HISWA (Holthuijsen et al. 1989) or the third-generation SWAN model (Holthuijsen et al. 1993). At each call to the WAVE module the latest bed elevations, water elevations, and if desired, current velocities are transferred from FLOW to the WAVE module.

Near-shore wave processes are taken into account, as follows: wave forcing due to breaking (by radiation stress gradients), which is modeled as a shear stress at the water surface; effect of the enhanced bed shear stress on the flow field (apparent bed roughness concept); wave-induced mass flux; additional turbulence production due to dissipation in the bottom wave boundary layer and due to wave white capping and breaking at the surface (extra production terms in the $k-\varepsilon$ turbulence closure model); streaming (wave-induced current in the bottom boundary layer directed in the direction of wave propagation), which is modeled as an additional shear stress acting across the thickness of the bottom wave boundary layer; infragravity wave motions; and nonlinear peak orbital velocities (Walstra et al. 2000). The inclusion of these processes is especially important for the accurate modelling of sediment transport in the near-shore coastal zone.

Suspended Sediments

An advection–diffusion equation is available to model constituents such as salinity, cohesive, and noncohesive suspended sediment. This 3D equation is written as

$$\frac{\partial[hC]}{\partial t}+\frac{\partial[hUC]}{\partial x}+\frac{\partial[hVC]}{\partial y}+\frac{\partial((\omega-w_s)C)}{\partial \sigma} = h\left[\frac{\partial}{\partial x}\left(\varepsilon_{s,x}\frac{\partial C}{\partial x}\right)+\frac{\partial}{\partial y}\left(\varepsilon_{s,y}\frac{\partial C}{\partial y}\right)\right]+\frac{1}{h}\frac{\partial}{\partial \sigma}\left[\varepsilon_{s,z}\frac{\partial C}{\partial \sigma}\right]+hS \tag{6}$$

where c=concentration; w_s=settling velocity of suspended sediment; S=source and sink terms per unit area; and ε_s=sediment diffusivity coefficients in x,y,z-directions. As regards the suspended sediment transport of clay, silt, and sand, the basic parameters are taken from the TR2004 model as presented in Part 2. Besides the algebraic turbulence closure according to the TR2004 formulations, the $\varepsilon_{s,z}$ coefficient (vertical diffusivity) can also be determined by the $k-\varepsilon$ turbulence model (including the β factor, see Part 2). If the $k-\varepsilon$ model is selected, this model is also used in the flow model (excluding the β factor). The horizontal diffusivity values are taken from the flow model. Possible fluid density differences (due to presence of sediments) can be taken into account coupled to the momentum and continuity equations.

Subgrid Model for Reference Concentration of Suspended Transport

The computation of the suspended sediment transport according to Eq. (6) is based on the concept of a reference concentration (bed boundary condition) very close to the bed. The reference concentration at level $z=a$ (approximately half the bed roughness) is extrapolated to the center of the first grid cell using an exponential function. To extrapolate the reference concentration value [Eq. (5) of Part 2] to the first grid point of the 3D model, a subgrid model is used which accounts for hindered settling, turbulence damping effects using a refined subgrid with 20 grid points in the lowest layer of the model and applying the function: $c_i=c_{i-1}\exp[-(w_{s,i-1}/\varepsilon_{s,i-1})(z_i+\Delta z_i)]$. The fall velocity and mixing coefficient are modified taking hindered settling and turbulence damping effects into account (see Part 2), based on values of the previous point (lower point i-1).

Bed Level Evolution

The bed level evolution is based on the sediment continuity equation (mass balance)

$$\frac{\partial(1-p)z_b}{\partial t}+\frac{\partial(S_{b,x}+S_{s,c,x}+S_{s,w,x})}{\partial x}+\frac{\partial(S_{b,y}+S_{s,c,y}+S_{s,w,y})}{\partial y}=0 \tag{7}$$

Eq. (7) can also be expressed as

$$\frac{\partial(1-p)z_b}{\partial t}+\frac{\partial(S_{b,x}+S_{s,w,x})}{\partial x}+\frac{\partial(S_{b,y}+S_{s,w,y})}{\partial y}+\left(\varepsilon_{s,z}\frac{\partial c}{\partial \sigma}-(\omega-w_s)c\right)_{\text{near-bed}}=0 \tag{8}$$

with: $S_{b,x,y}$=bed-load transport (by volume) in x,y-direction (u,v-velocity direction), Part 1, $S_{s,c,x,y}$=current-related suspended transport (by volume) in the x,y-direction (Part 2); $S_{s,w,x,y}$=wave-related suspended transport (by volume) in the x,y direction (Part 2); $\varepsilon_{s,z}$=mixing coefficient at lowest grid point; w_s=settling velocity; c=concentration; and p=porosity.

The last term of Eq. (8) represents the vertical sedimentation and erosion terms at the upper interface of the lowest grid cell based on the computed concentration in the cells and concentration gradient across the cell (handled by source and sink terms, which are updated each half time step). The bed boundary condition always is a prescribed reference concentration based on Eq. (5) of Part 2. The reference concentration at level $z=a$ (approximately half the bed roughness) is extrapolated to the center of the first grid cell (see above). The bed–load transport contributions are based on a quasi-steady intrawave approach, which implies that the bed–load transport is assumed to respond almost instantaneously to orbital velocities within the wave cycle including the prevailing current velocity. Similarly, the wave-related suspended-load transport contribution ($S_{s,w}$) is assumed to respond almost instantaneously to the orbital velocities. This transport contribution can be formulated in terms of time-averaged (over the wave period) parameters resulting in a relatively simple transport expression, as explained in Part 2.

The current-related suspended-load transport is based on the variation of the suspended sand concentration field due to the effects of currents and waves. Using a 2DH approach, the sand concentration field is described in terms of the depth-averaged equilibrium sand concentration derived from equilibrium transport formulations and an exponential adjustment factor based on the (numerical) method of Galappatti (1983). This latter method is based on using first-order adjustment functions to represent the phase lags between the depth-averaged concentrations and depth-averaged velocities. Using a 3D approach, the sand concentration field is based on the numerical solution of the 3D advection–diffusion equation [Eq. (6)]. In the latter approach, the current-related suspended transport components are defined as

$$S_{s,c,x}=\int_a^h\left(uc-\varepsilon_{s,z}\frac{\partial c}{\partial x}\right)dz$$

$$S_{s,c,y}=\int_a^h\left(vc-\varepsilon_{s,z}\frac{\partial c}{\partial y}\right)dz \tag{9}$$

All the transport formulations contain calibration factors (input values): f_{BED} (on the bed–load transport), f_{SUS} (on the reference concentration), and f_{SUSW} (on the wave-related suspended transport). These factors are applied as constants in the spatial and temporal domain. Default values are 1, which implies that the formulations represent the physics of the sand transport process perfectly. Lower and upper limits of the scaling factors are 0.5 and 2. Using these factors, the user of the model can up or downscale the transport rates to calibrate the model if transport data and/or bathymetry data are available.

The 3D model can be operated in rectangular or in curvilinear grid mode, in line mode or in area mode and in single-layer (depth-averaged; 1DH or 2DH) or multilayer (2DV or 3D) mode with an online coupling between hydrodynamic and transport/bottom modules which implies that the flow, transport, and bottom updating are now merged into one online model, only the wave model is executed separately (data communication between online model and wave model). The online coupling involves that the transport and bottom updating is performed at every flow time step. The bed evolution can be upscaled (accelerated) after each time step by means of a so-called morphological upscaling factor

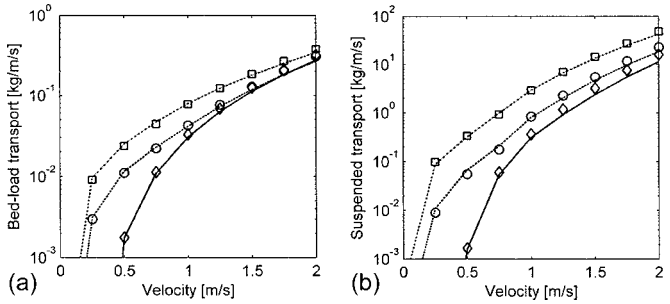

Fig. 1. Computed bed load (a) and suspended load (b) transport: solid line=TR2004 model (H_s=0 m); dashed line=TR2004 model (H_s=1 m); dotted–dashed line=TR2004 model (H_s=2 m); diamond=3D model (H_s=0 m); open circle=3D model (H_s=1 m); and open square=3D model (H_s=0 m)

(MSF) (e.g. with MSF=100, a morphological prediction based on a tidal cycle of 12.5 h would represent 12.5×100 h=52 days). The morphological upscaling factor has to be prescribed by the user and depends on the dynamic response of the area of interest; dynamic areas require a lower MSF value whereas for more stable environments the MSF can be increased (typical range is between 10 and 1,000 for dynamic and stable areas respectively).

Comparison of Bed-Load and Suspended-Load Transport by 3D Model and TR2004

To evaluate the depth-integrated transport rates (including bed-load transport) computed by the 3D model (version February 2006) in comparison to those of the stand-alone model TR2004, these values have been computed for a water depth of 5 m and a median particle size of 250 μm (d_{10}=125 μm and d_{90}=500 μm) as presented in Part 2 (see Fig. 20 of Part 2). The depth-averaged current velocity is up to 2 m/s. The significant wave height (H_s) is between 0 and 2 m and wave periods between 5 and 7 s. The wave direction is normal to the coast, whereas the current is parallel to the coast (φ=angle between waves and current directions=90°). Similar results for other angles are given by van Rijn et al. (2004). The temperature is 15°C and the salinity is 0. The (longshore) transport rates of the TR2004 model and the 3D model are shown in Fig. 1 for H_s=0, 1, and 2 m. The computed transport rates are in very good agreement in the low velocity range up to 1 m/s. For velocities in the range of 1–2 m/s the maximum errors are of the order of 50% due to small differences in the computed velocities near the bed. The near-bed velocities of the 3D model are slightly larger than those of the TR2004 model, the latter being based on a logarithmic model approach, whereas the 3D model solves the momentum equation. Furthermore, the subgrid model of the 3D model to compute the concentrations near the bed is based on 20 grid points only (to reduce the computational time), whereas the TR2004 uses much more grid points to represent the detailed processes (hindered settling and turbulence damping effects) near the bed leading to small differences between both models. As computer power increases, the number of grid points of the subgrid model can also be increased to improve the model accuracy. At present stage of research, the overall accuracy of the transport model of 3D is supposed to be sufficient for daily engineering practice, as is shown below for various morphodynamic verification cases.

Verification Studies

Methodology

The DELFT3D-model and the CROSMOR2D-model have been upgraded with the TR2004 transport formulations. The most important improvements involve the inclusion of a bed roughness predictor and refinement of the predictors for the suspended sediment size and the near-bed reference concentration (Parts 1 and 2) and the extension of the model to the clay and silt range. The verification cases are the following: (1) a laboratory experiment concerning a trench normal to flow and parallel to waves; (2) two large-scale laboratory experiments concerning bed profile (bar) behavior in the coastal surf zone; (3) Scheveningen trench in North Sea (The Netherlands); and (4) artificial sand ridge near Scheveningen in North Sea (The Netherlands).

In many verification studies of morphodynamic models there often is a tendency to focus on the bed evolution only, without providing information on the reliability of the sediment predictors, mainly because sand transport data are often lacking. Herein, it is proposed to make a clear distinction between predictions based on up or down scaling of the observed sediment transport rates and based on calibration of the observed morphological changes. The former approach implies that the sand transport rates upstream of the location of interest should be known (measured), while the latter approach is based on known bed level changes. To assess the model performance, the RMS error and the Brier skill score (BSS) have been used (see van Rijn et al. 2003). The BSS compares the predicted bed levels with the measured bed levels and a reference or baseline bed level prediction. The baseline prediction for morphodynamic modeling will usually be that the bed remains unaltered. In other words it means that the initial bathymetry is used as the baseline prediction for the final bathymetry. A score of BSS=1 implies perfect agreement. If the model prediction is further away from the final measured condition than the baseline prediction, the skill score is negative. Van Rijn et al. (2003) provide the following qualifications: BSS =0.8–1: excellent; BSS=0.6–0.8: good; BSS=0.3–0.6: fair; BSS=0–0.3: poor and BSS<0: bad. The BSS is not a very good discriminator for small migration rates and directions (Case 3). Further details and discussion of the use of the BSS for evaluating coastal morphodynamic modeling were given by Sutherland and Soulsby (2003) and Sutherland et al. (2004).

Case 1: Trench Normal to Flow and Parallel to Waves in Laboratory Basin

The experiment has been carried out in a wave-current basin (van Rijn and Havinga 1995). A channel (width of 4 m) with a sediment bed consisting of fine sand (d_{50}=100 μm; d_{90} =130 μm; settling velocity=6 mm/s) was present at the end of the basin. The bed surface of the channel was at the same level as the cement floor of the surrounding basin. Irregular waves were generated by a directional wave generator. The wave spectrum (JONSWAP form) was single topped with a peak frequency of 0.4 Hz. The water depth was about 0.42 m. The wave direction was 90° (angle between wave orthogonal and current direction). The significant wave height was 0.105 m and the peak wave period was 2.2 s. A pump system was used to generate a current in the channel (depth-averaged flow velocity=0.245 m/s). Guiding boards were used to confine the current in the movable-bed channel (width 4 m). The guiding boards were placed normal to the wave crests to allow free passage of the waves. The vertical dis-

Table 1. Model Settings Used in the Sensitivity Runs for Case 1

Run	Scaling factor	Transport formula	Sediment mixing	Suspended sediment size	Roughness	Error in bed level	
						RMS (m)	BSS (exc.)
H01	1.49	TR2004	K-ε model	TR2004	TR2004	0.015	0.95
H02	1.05	TR2004	TR2004	TR2004	TR2004	0.019	0.93
H03	0.78	TR2004	TR2004	$d_s=0.8d_{50}$	TR2004	0.027	0.86
H04	1.61	TR2004	TR2004	TR2004	$k_{s,c}=k_{s,w}=0.01$ m	0.016	0.95
H05	4.20	TR1993	TR1993	$d_s=0.8d_{50}$	$k_{s,c}=k_{s,w}=0.01$ m	0.018	0.93

tribution of the velocity in the middle of the channel was perfectly logarithmic (current alone). The main axis of the trench was perpendicular to the main current direction. The trench dimensions are shown in Fig. 2. The suspended sand transport upstream of the trench was measured to be 0.022 kg/s/m. A two-dimensional-vertical (2DV) model was constructed to simulate the processes in the longitudinal center line of the flow. For each run the computed transport rate at the inlet was scaled (made equal) to the measured upstream value. In vertical direction the grid consists of 10 layers with a high resolution near the bed which decreases towards the water surface. The morphological upscaling factor is set to MSF=90 to reduce the computational time (Walstra et al. 2004).

The settings of the runs are shown in Table 1. The base run is H02, which uses all the defaults according to TR2004. A scaling factor of 1.05 (very close to the default value of 1) was required to obtain the measured upstream suspended transport rate. The 3D model can either use the vertical sediment mixing parametrization of TR2004 or use the $k-\varepsilon$ turbulence model, this was tested in Run H01. The settling velocity is an important parameter, which determines the amount of sediment in suspension and as a consequence the back filling of the trench. The settling velocity is determined by the median diameter of the suspended sediment (d_s), which can be used as a constant value (see run H03, Table 1) or predicted by the model (see Part 2). Run H04 has a constant bed roughness (about equal to the ripple height) instead of the roughness predictor (Run H02). Finally, a simulation was executed with TR1993 formulations with default settings (Run H05).

Fig. 2 presents computed and measured bed levels after about 25 h for all runs, showing that the model gives a satisfactory agreement for all model settings. This is confirmed by the statistic parameters shown in Table 1. The averaged RMS error is about 0.015–0.020 m, which is less than 10% of the initial pit depth. The BSSs of all simulations can be characterized as "excellent" having values higher than 0.8. This illustrates the robustness and accuracy of the advection–diffusion solver of the 3D model. By using scaled upstream transport rates, the modification of transport settings of TR2004 only has a limited effect on the morphological development. This implies that the scaling factors listed in Table 1 are the main arbitrators for the quality assessment of the TR2004 transport formulation. Comparison of these factors shows that TR2004 gives the best prediction having a scaling factor (1.05 in Run H02) closest to one. Also the TR2004 roughness and suspended sediment size predictors and the sediment mixing parameterization result in a better prediction.

Case 2: Large-Scale Laboratory Experiments on Cross-Shore Transport and Bed Profile Changes

Two tests from the LIP experiments (Sánchez-Arcilla 1995) have been used to verify the 2D CROSMOR-model. Test 1B simulates a storm condition with a breaker bar in the surf zone moving in offshore direction (offshore event). Test 1C simulates a typical swell condition (poststorm) with a breaker bar in the surf zone moving in onshore direction (onshore event). The bed material consists of sand with $d_{10}=150$, $d_{50}=200$, and $d_{90}=400$ μm. The offshore water depth (h_o) to still water level is 4.1 m in all tests. The basic hydrodynamic data are given in Table 2. The measured bed profiles at the beginning and at the end of the tests are shown in Figs. 3 and 4. The computed bed profiles are also shown. The model is run in standard mode with all cross-shore wave, flow, and sand transport processes included. The computed wave-related net sand transport rates (due to wave asymmetry) are found to be in onshore direction, when the phase lag effects on sand transport processes are excluded (see Part 2). The wave-breaking induced undertow causes offshore-directed sand transport rates. Bed level changes depend on the gradients of the balance of these two transport components. As can be observed in Figs. 3 and 4, both offshore (1B) and onshore (1C) bar movements can be simulated reasonably well in qualitative sense (BSSs are in the range of fair to good, see Table 2). The effect of the wave-induced fluid acceleration in asymmetric waves on the bed-shear stress (see Part 1) and hence on the bed-load transport has been included in Runs B1 and C1 (Nielsen and Callaghan 2003). The erosion landward of the outer bar (between 143 and 157 m) is simulated rather well for Test 1B. The eroded sand is transported in seaward direction to form a breaker bar at 135 m. The model bar does not move sufficiently in seaward direction for Test 1B (Fig. 3); the observed bar behavior is better simulated if the acceleration effects are neglected. Fluid acceleration effects do not seem to be very important for breaking wave conditions, because wave asymmetry is suppressed in breaking wave conditions. The model also predicts an inner bar (at 160 m) with sand eroded from the beach for Test 1B; the measured bed profile does not show this behavior. The onshore bar event (1C) is reasonably well simulated by the model due to inclusion of wave-asymmetry on the bed-load transport for Test 1C (Fig. 4). The inclusion of the acceleration effect on the bed-load transport improves the prediction. Neglecting the streaming effect near the bed, has almost no effect on the computed bed profiles (not shown; bed profiles with and without on top of each other). The bed profile of Test 1C was almost fully covered with small-scale wave ripples, which may lead to offshore-directed transport processes particularly under regular waves (Nielsen 1988, 1992; Van der Werf 2006). A run including these effects was made to determine the net offshore-directed transport rates and associated bed profile changes. The maximum negative (offshore-directed) transport rate is found to be about −0.1 kg/s/m at the bar crest ($x=135$ m), which is a value quite similar to the values measured in rippled bed conditions by Van der Werf (2006). As can be observed in Fig. 4, offshore-directed wave-related transport rates due to phase lag effects lead to strong offshore migration of the bar which has not

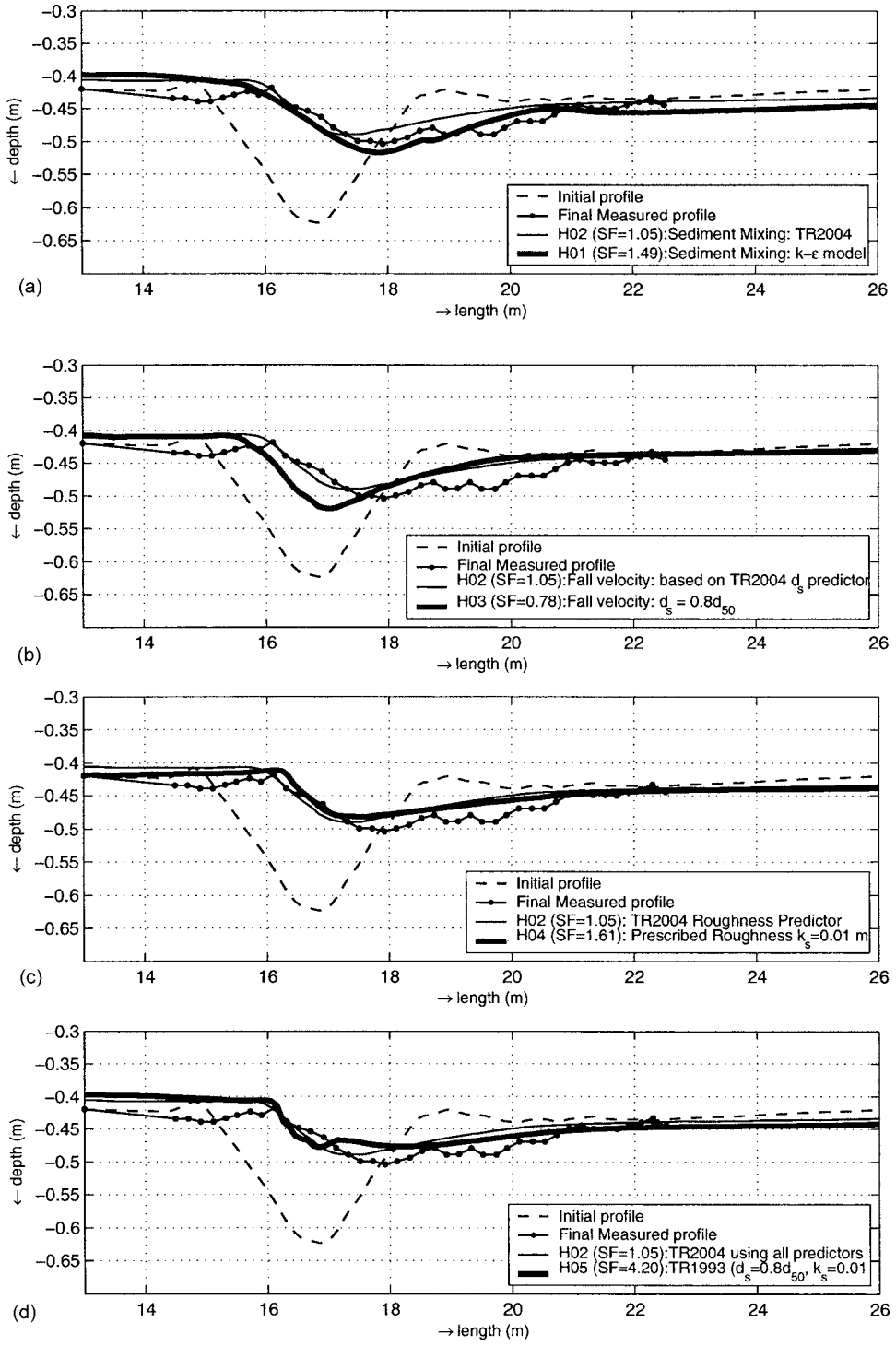

Fig. 2. Morphological development of trench for (a) comparison using different sediment mixing relations; (b) TR2004 suspended sediment size predictor versus constant factor; (c) TR2004 roughness predictor versus prescribed roughness height; and (d) comparison of transport formulations TR2004 versus TR1993

been observed (BSS <0). This result shows that the presence of offshore-directed transport rates due to wave motion over ripples is not realistic for Test 1C (similar for Test 1B, not shown). Probably, the bed ripples are not steep enough under irregular waves to generate strong vortex motions with phase lags between sediment concentration and orbital velocity. Summarizing, the model runs show that the sediment transport model (neglecting phase lags) can simulate the qualitative aspects of the inner surf zone dynamics reasonably well. Fluid acceleration effects on bed-shear stress and hence on sand transport appear to be important for low wave conditions, but not for storm conditions (breaking waves). It is most important to model the onshore-directed wave asymmetry transport and the offshore-directed transport by the undertow correctly. Phase lag effects influencing the wave-related transport do not seem to be very important under irregular waves.

The present model is far from perfect for the inner surf and swash zone, but it can be used in these conditions as a hindcast model. The user has to decide which of the processes should be

Table 2. Data of Large-Scale Laboratory Experiments for Case 2

Tests	Runs	Offshore significant wave height $H_{s,o}$ (m)	Offshore significant wave period T_p (s)	BSS (between $x=120$ m and $x=160$ m)
1B	Run B1 including acceleration effect	1.4	5	0.47 (fair)
1B	Run B2 excluding acceleration effect	1.4	5	0.74 (good)
1C	Run C1 including acceleration effect	0.6	8	0.72 (good)
1C	Run C2 excluding acceleration effect	0.6	8	0.64 (good)

included by using various input switches. Using this approach, a sensitivity study can be done to evaluate which processes are dominant. Sediment transport and associated morphological predictions cannot be done with great accuracy for the complicated inner surf and swash zone, especially not under fair-weather conditions when transport rates are low. However, it is possible to predict ranges of variation over short term time scale (storm scale) in conditions with dominant suspended-load transport, but not on the seasonal time scale (van Rijn et al. 2003) being a combination of low and high wave conditions. The basic problem is that the net transport in the inner surf and swash zone is a delicate balance of various onshore and offshore-directed transport processes which are all of the same order of magnitude. Thus, the net result in these conditions is by definition uncertain and almost unpredictable (van Rijn et al. 2003). Much more research is required to fully understand these effects and the associated breaker bar behavior under storm and poststorm conditions.

Case 3: Scheveningen Trench in North Sea, The Netherlands

A trial trench was dredged in the North Sea bed (sand with $d_{50}=200$ μm, $d_{10}=150$ μm, $d_{90}=300$ μm) near the town of Scheveningen (see Figs. 5 and 9) in March 1964 to obtain information of deposition rates with respect to the construction of a future sewer-pipeline trench (Svasek 1964). The trial trench was dredged perpendicular to the shoreline at a distance between 1 km

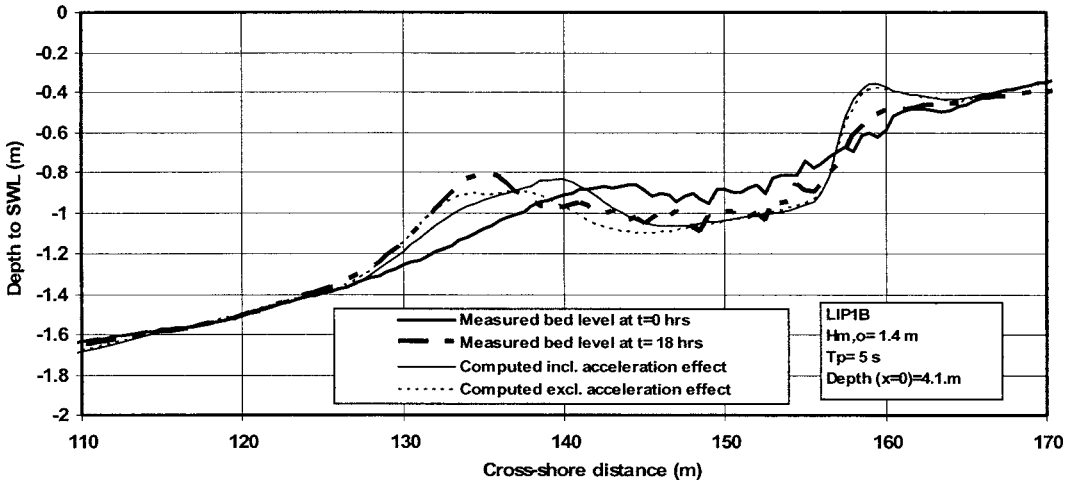

Fig. 3. Measured and computed bed profiles for offshore bar experiment (LIP1B)

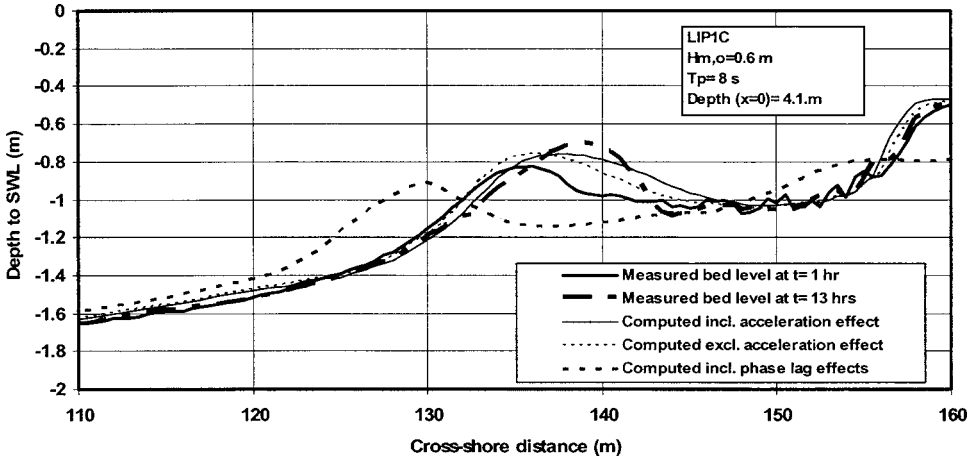

Fig. 4. Measured and computed bed profiles for onshore bar experiment (LIP1C)

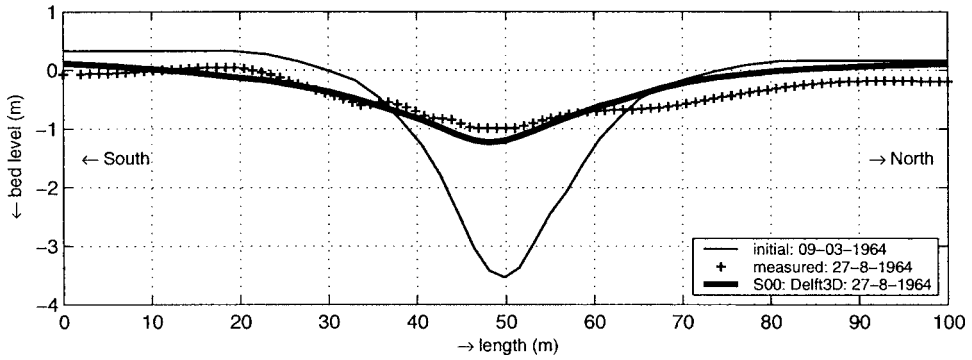

Fig. 5. Comparison of measured and computed bed profiles of Base Run S00

(local depth of about 7 m below MSL) and 1.7 km (local depth of 8 to 11 m) from the shoreline. The length of the trench along the main axis of the trench was about 700 m; the initial trench dimensions are given in Fig. 5. The dredged volume was about 30,000 m^3. The local peak flood velocity is about 0.6 m/s and the ebb velocity is about 0.5 m/s parallel to the shoreline (and thus perpendicular to the trench axis). The tidal range is about 1.5 m. The trench was sounded regularly in the period between March 7 and August 27, 1964. A few summer storms occurred during this observation period. Analysis of the bed profiles shows that the filling of the trench is almost symmetric without net migration. The deposition rate is about 30–35 m^3/m over 173 days (March 7 to August 27, 1964).

Two model schematizations are considered: a line model across the trench (line 2 parallel to coast in area) in about 8 m of water (1DH and 2DV) and an area model (2DH and 3D) covering the entire area of interest (Walstra et al. 2004). The line model was used to perform a large number of sensitivity simulations studying the effect of different boundary conditions for tide and waves. Both models were used in single-layer mode (depth-averaged) and in multilayer mode (2DV or 3D; 10 layers). Both models were driven with boundary conditions obtained from a large scale coastal model (HCZ model) (Roelvink et al. 2001). The neap–spring tidal cycle is represented by a representative (morphological tide), which gives an accurate estimate of the residual transports in this area (MSF=27.5). A wave exceedance table with wave height and wave period data was available for the considered period. However, no wave directions were available. This wave exceedance table was correlated to wind measurements to reconstruct a time series of waves. The wave height was assumed to be normal to the coast and constant in the model domain without inducing any wave driving currents (no breaking waves in relatively deep water).

As no transport measurements were available for this site, field data from a nearby site obtained during the SANDPIT Project (van Rijn et al. 2005) were used to calibrate the upstream (at the model boundary) suspended transport rates. Based on analysis of the field data, a condition typical for Scheveningen(H_s=significant wave height=1.3 m, T_p=peak wave period=5.5 s, depth=8 m, and longshore velocity=0.6 m/s) resulted in a "measured" depth-integrated suspended transport of 0.165 kg/m/s. This value was used to scale the upstream transport rate for all Scheveningen simulations resulting in scaling factors in the range of 1.5–1.8 to obtain the measured transport value (Table 3).

Table 3 presents an overview of all sensitivity runs involved: the sediment mixing was varied (S01), the reconstructed wave time series was used (S07), a residual flow of 0.07 m/s was added to the tidal velocity signal (S03), a depth-averaged run was made (S04). To illustrate the effect of the transport scaling, a simulation was carried out with no scaling of the transports (S08). Furthermore, two area model runs in 2DH (S22) and 3D (S33) were made using the settings of reference run (S00). The scaling factors in the range of 1.5–1.8 (see Table 3) show that TR2004 gives a fairly good estimate of the measured transports.

Fig. 5 presents simulation results of the Base Run S00 based on the TR2004 sand transport model. Run S01 with the k-ε turbulence model for the mixing coefficients gives similar results. This is also illustrated by the statistic parameters shown in Table 3. The RMS error is about 0.20 m which is only 5% of the initial

Table 3. Model Settings Used in the Sensitivity Runs for Case 3

Run	Scaling factor	Dimension	Sediment mixing	Wave climate	Tide	Errors in bed level	
						RMS (m)	BSS (exc.)
S00	1.56	2DV; multilayer	TR2004	Constant	No residual	0.22	0.94
S01	1.68	2DV; multilayer	k-ε	Constant	No residual	0.20	0.95
S07	1.56	2DV; multilayer	TR2004	Varying	No residual	0.32	0.90
S03	1.56	2DV; multilayer	TR2004	Constant	With residual	0.52	0.85
S04	1.77	1DH; single-layer	TR2004	Constant	No residual	0.30	0.92
S08	1.00	2DV; multilayer	TR2004	Constant	No residual	0.47	0.80
S22	1.77	2DH; single-layer	TR2004	Constant	No residual	0.32	0.92
S33	1.56	3D; multilayer	TR2004	Constant	No residual	0.31	0.93

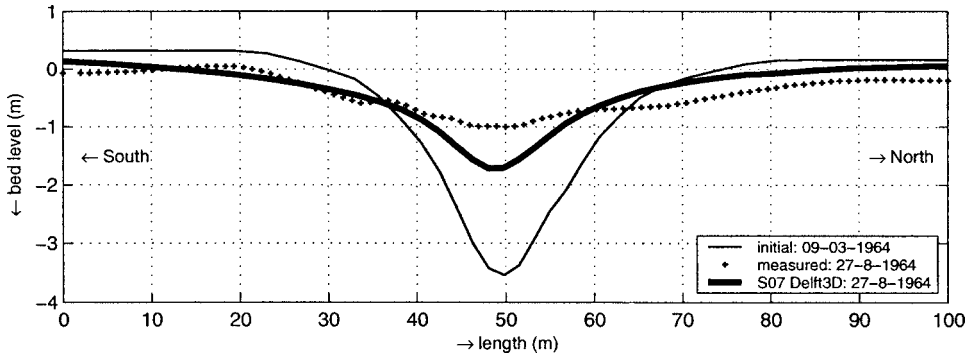

Fig. 6. Comparison of measured and computed bed profiles of Run S07

trench depth. The BSSs are about 0.9 which qualify these simulations as "excellent." Fig. 6 shows the simulation using the reconstructed wave time series. The observed sedimentation of the trench is slightly underestimated. Analysis of the results shows that the sedimentation in this latter run is relatively large during the higher wave conditions whereas the sedimentation in the run with the constant wave height is occurring more gradually. The sensitivity of the model for the higher wave conditions implies that an accurate prediction can only be made if the reconstructed wave time series is reliable. Fig. 7 shows the development of the trench if a residual tidal current of 0.07 m/s is added to the tidal signal. This results in a significant overestimation of the migration and sedimentation of the trench. Using the depth-averaged model which is based on an exponential approach for the adjustment of the suspended sediment transport (Galappatti 1983), the trench is almost completely filled up (overestimation, not shown). Using the model without scaling of the upstream suspended transport, the sedimentation is under-estimated (not shown). In fact, it is only the morphological time scale which is now different, running this simulation for about 9 months instead of 6 (i.e., applying the scaling factor of the reference run) would result in a similar prediction as that of the reference run (S00). Finally, the results of the area models (2DH and 3D) interpolated along the same cross section (line 2) are shown in Fig. 8. The sedimentation is slightly overestimated by the 2DH and 3D models, but the overall agreement is excellent (BSS $>$ 0.9). The predicted sedimentation patterns along the trench also are in good agreement with observed patterns (not shown). The simulations for the Scheveningen trench again show that with reliable hydrodynamic boundary conditions and scaling the transports to realistic values a very good estimate can be given of the morphological development of a trench. All the simulations can be qualified excellent or good with BSSs generally higher than 0.8, using the ranges given by van Rijn et al. (2003). It may be argued whether the results of Figs. 6

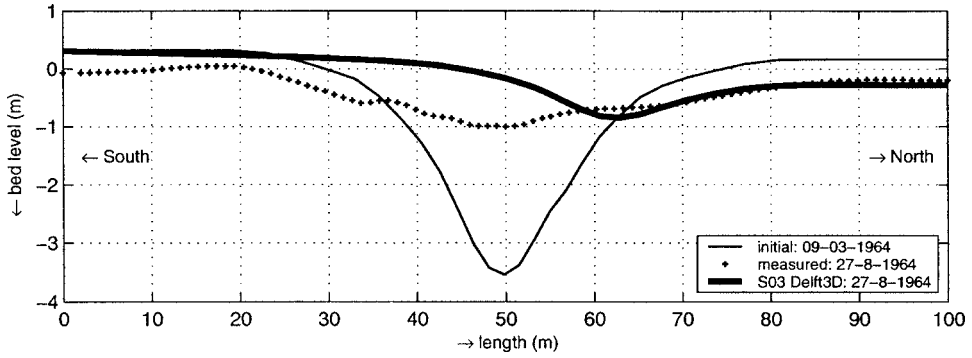

Fig. 7. Comparison of measured and computed bed profiles of Run S03

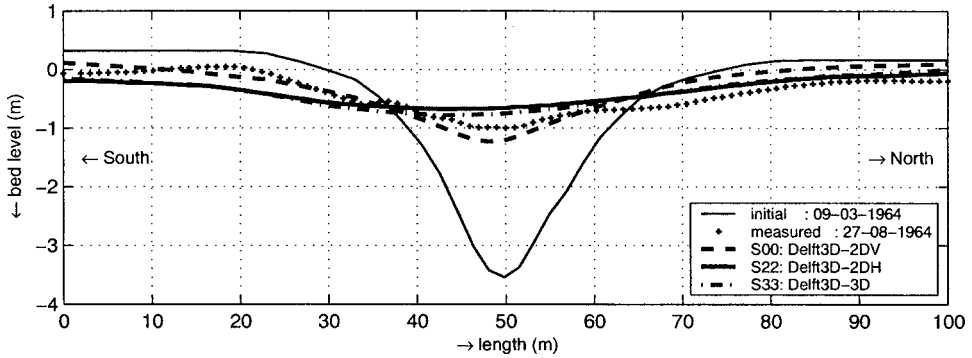

Fig. 8. Comparison of measured and computed bed profiles of using the model in 2DH, 2DV, and 3D modes

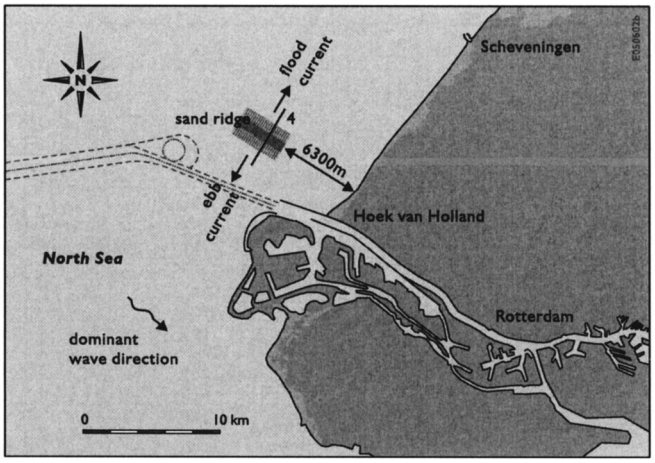

Fig. 9. Plan view of the location of the artificial sand ridge

and 7 really are excellent. Based on visual evaluation, it would be more appropriate to judge these results as fair to good.

Case 4: Artificial Sand Ridge near Hoek van Holland in North Sea, The Netherlands

From 1982 to 1986 an artificial sand ridge was created by dumping sand (3.5 million m^3) onto the shoreface at the location of Hoek van Holland immediately north of the navigation channel to the Port of Rotterdam (Van Woudenberg 1996). The ridge had a length of a few km's normal to the shore and to the peak tidal current direction (about 0.6 m/s to north and about 0.5 m/s to south; tidal range of 1.5–2 m) in an area with depths between 15 and 23 m (see Fig. 9). Ridge dimensions after creation of the ridge were: length of about 3,600 m; toe width between 250 and 370 m; height between 1.3 and 4 m; slopes between 1:50 and 1:100 on the south flank and between 1:20 and 1:50 on the north flank; d_{50} between 150 and 450 μm. The landward end of the ridge is about 6,300 m from the shoreline. The bar is perpendicular to the coast and to the tidal flow (flood flow to north, ebb flow to south). From 1982 to 2000 the morphological development of the ridge was monitored regularly (vertical inaccuracy of 0.1–0.2 m). As dredging was carried out on the seaward side of the ridge, the attention herein is focused on the shallower part of the ridge (Section 4 in eastern part of site, Fig. 9). The main findings of the data analysis for Section 4 are: average decrease in height of the ridge of about 1 m over period 1986–2000 and an average northward migration (in the direction of the dominant flood current) of about 50 m over the same period.

The 3D model was used in line mode (Cross-section 4, see Fig. 9) with a single layer (depth averaged; 1DH approach) and with multilayers (20 layers; 2DV approach), covering a period of 1986–2000. The particle size of the bed material is set to d_{10} =240 μm, d_{50}=300 μm, and d_{90}=600 μm (standard runs). The vertical eddy diffusivity is represented by the algebraic model based on TR2004; the horizontal eddy diffusivity is set to a constant value of 1 m^2/s. Boundary conditions were taken from the same large scale HCZ-model as used for Case 3. Locally, the grid mesh of the nested model was refined to obtain the required resolution in the ridge area (minimum grid size of 12 m in alongshore direction and about 100 m in cross-shore direction). The salinity at the seaward boundary is 31 ppt. The water temperature is 15°C. Wind waves are simulated as a constant wave height in the spatial domain based on the results of an earlier study (Walstra et al. 1997): H_s=2.25 m, T_p=6.6 s, and direction 315° to north and percentage of occurrence=84%. Sensitivity results based on a constant wave height and a detailed wave spectrum are shown by Tonnon et al. (2007). They have concluded that the long term morphological development of the ridge can be simulated quite well by using a single, constant representative wave height (2.25 m) and direction. To reduce the computational time, the neap–spring tidal velocity cycle with waves superimposed has been reduced to a representative (so-called morphological tide with one flood and ebb velocity cycle taken from the neap–spring cycle), producing a net annual transport rate of about 18 $m^3/m/year$ in the (undisturbed) region south of the ridge crest (at depth of about 18 m) similar to that of the full neap–spring

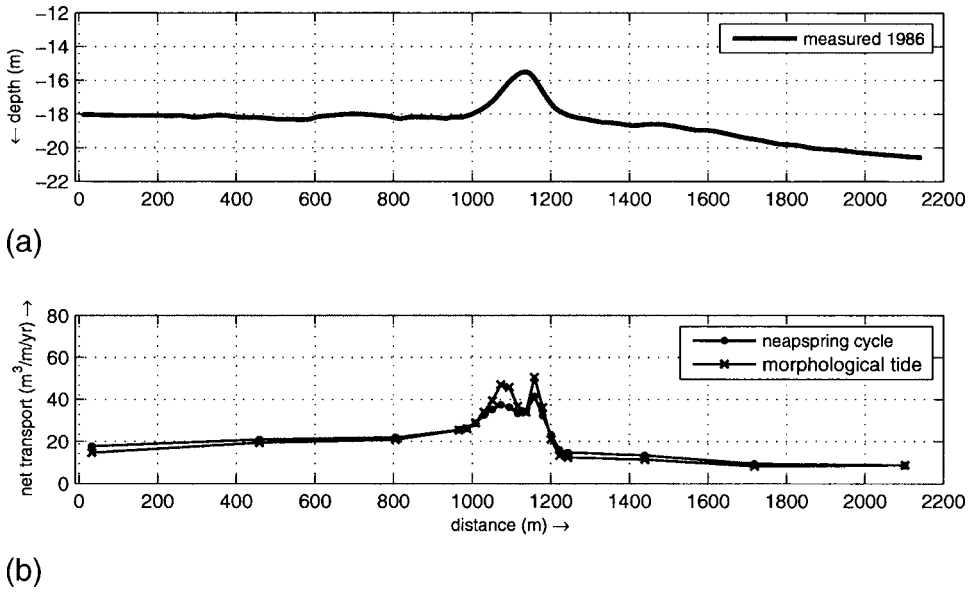

Fig. 10. Net transport rates (b) based on morphological tide and based on full neap-spring tidal cycle and the ridge morphology of 1986 [initial situation, (a)]

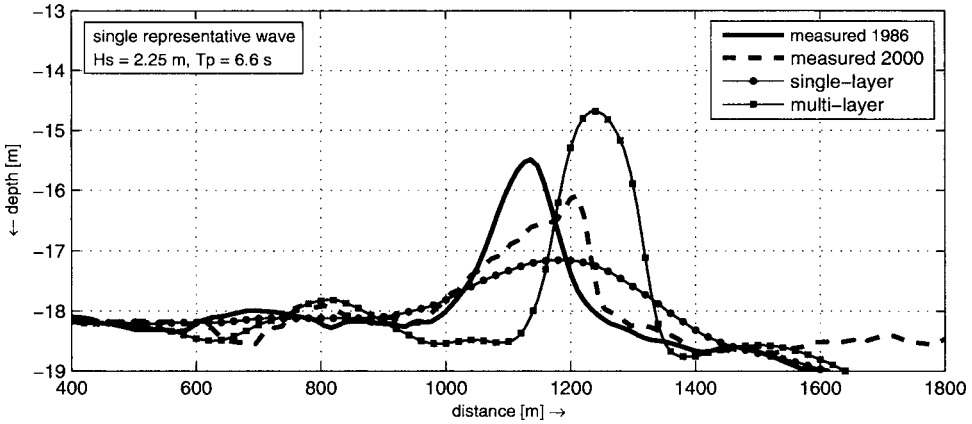

Fig. 11. Bottom profile development of Section 4 between 1986 and 2000 using single layer (depth-averaged model, 1DH) and multilayer approach (2DV)

cycle (Tonnon et al. 2006), see Fig. 10. The computed net annual transport rate (18 $m^3/m/year$) on the south side of the ridge is in the range of 15 ± 10 $m^3/m/year$, as given by van Rijn (1997). The morphological tide overpredicts the net transport rates at the ridge crest.

The model runs show growth and decay of the ridge height (see Figs. 11–13) depending on the bed roughness and the bed material diameter, which both strongly affect the ratio of bed load and suspended-load transport. The basic cause of ridge growth is the deformation of the velocity profiles along the ridge morphology resulting in a vertical circulation cell with net (time-averaged) velocities toward the ridge crest in the near-bed region. In the case of dominant bed-load transport (particle diameter of 300 μm) this results in a constant flow of sediments to the ridge crest. The effect of ridge growth can only be represented by using a multilayer model (2DV or 3D) resolving the vertical structure of

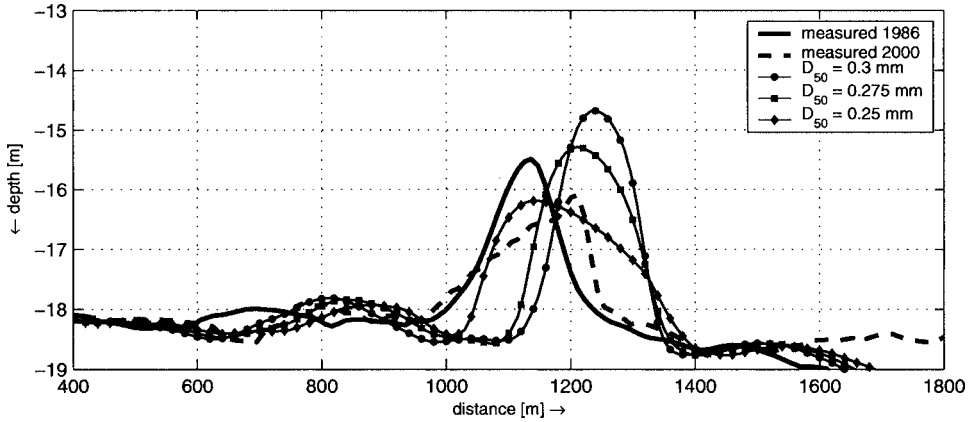

Fig. 12. Bottom profile development of Section 4 between 1986 and 200u using a median sediment diameter (d_{50}) of 0.3, 0.275, and 0.25 mm

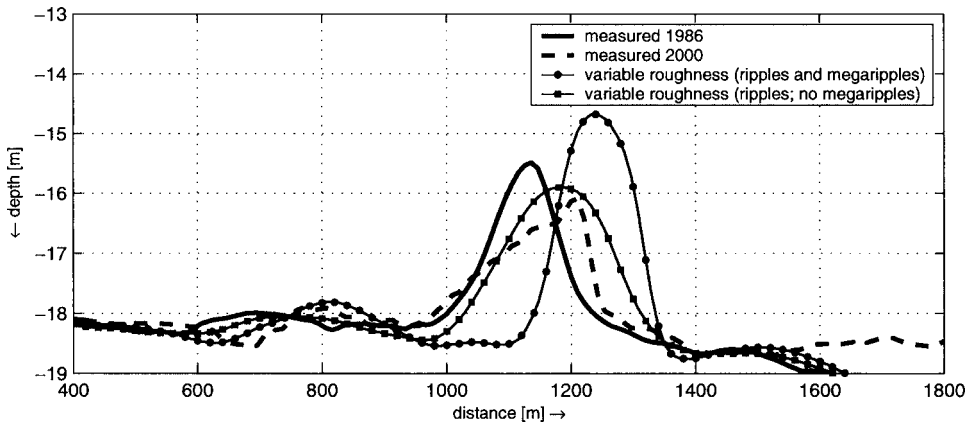

Fig. 13. Bottom profile development of Section 4 between 1986 and 2000 using variable bed roughness (predictor) with and without megaripple roughness

Table 4. Model Settings Used for Case 4

Run	Particle size (μm)	Bed roughness predictor	Dimension	Errors in bed level [RMS (m)]
R1	300	Variable including megaripples	Multilayer, 2DV	1.30
R2	300	Variable including megaripples	Single layer, 1DH	0.45
R3	275	Variable including megaripples	Multilayer, 2DV	1.00
R4	250	Variable including megaripples	Multilayer, 2DV	0.55
R5	300	Variable excluding megaripples	Multilayer, 2DV	0.45

the flow (see Fig. 11). A single-layer depth-averaged model (1DH) cannot represent this phenomenon, as shown in Fig. 11. The results of the single layer model producing a relatively small RMS error (see Table 4) should be considered with care, as this model can only deal with a decaying type of ridge behavior.

Fig. 12 shows the bed evolution between 1986 and 2000 for three different sediment diameters in the range of 250–300 μm (0.25–0.3 mm). The sediment diameter affects the net annual transport rate and the ratio of bed load and suspended-load transport and hence the morphological evolution. The sediment diameter has a significant effect on the value of the net annual sand transport south of the ridge: 18 $m^3/m/year$ for $d_{50}=300$ μm (standard case), 23 $m^3/m/year$ for $d_{50}=275$ μm, and 31 $m^3/m/year$ for $d_{50}=250$ μm. Significant ridge growth can be observed for the largest diameter of 300 μm, because bed-load transport dominates for this case. The computations using finer sediments lead to a decrease of the ridge height, because a smaller sediment diameter leads to a larger contribution of suspended-load transport resulting in fattening of the ridge.

Finally, two runs are discussed, using a variable bed roughness with and without the effect of megaripples (this latter effect is optional for the model user). This latter assumption (no megaripple roughness effect) leads to larger C values in the range of 75–85 $m^{0.5}/s$ (smoother bed) and smaller bed-shear stresses, and hence, a smaller net annual transport rate of about 11 $m^3/m/year$ (south of the ridge). Fig. 13 shows reasonably good agreement between the measured and computed bed evolution after 15 years (no megaripples). These C values of 75–85 $m^{0.5}/s$ for a depth of 18–20 m result in k_s values in the range of 0.005 to 0.015 m (small-scale ripples; almost flat bed). Analysis of detailed bed level soundings (Van Woudenberg 1996) shows the presence of megaripples at the south flank of the ridge. Van Dijk and Kleinhans (2005) have observed that megaripples migrating over sand waves are common features in the North Sea, but they have also observed seasonal variations in the presence of megaripples, depending on the occurrence of storms. Megaripples tend to be washed out during stormy seasons. It seems that these latter effects are insufficiently taken into account by the new bed roughness predictor.

Overall, it is concluded that the detailed processes of ridge morphology over a long term period of 14 years can be represented reasonably well provided that the bed material size and the bed roughness are correctly modeled. The ridge migrates in the correct direction and the migration also is of the correct magnitude (about 50 m). The smallest RMS error is of the order of 0.5 m (see Table 4), which is about 20% of the initial ridge height. The results also show that the precise particle size variation and bed roughness variation along the ridge is of importance, because it changes the relative importance of bed-load transport and suspended transport along the sand ridge. Herein, a constant particle size has been used, but the use of a multifraction approach (as proposed in Part 3) with coarser sand (400 μm) on the ridge crest and finer sand (200 μm) on the flanks may give a better description of the more peaked shape of the ridge. These types of computations will be explored in future research.

Application of 3D Model

The 3D model is applied to two other complicated flow and sediment systems: steady flow along a spurdike (groyne) in a river, and tidal flow in the Yangtze Estuary with cohesive sediments in China.

River Flow along a Spurdike

This case is of great practical value concerning the flow and scour around a spurdike, which is often used in river flow to confine the flow to a narrower and deeper stream for navigation or to protect the embankment of the river against erosion. A typical phenomenon of a spurdike (or groyne) is the generation of local scour around the tip of the dike where the flow velocities accelerate and decelerate to pass around the obstruction in the flow. Often bed protection measures are necessary to minimize the scour effects. For example, Richardson (1988) observed a maximum scour depth of about $d_{s,max}=3h_o$ with h_o=upstream water depth for relatively long dikes (groynes) with $L/h_o>25$ (L=length of dike) in the Mississippi River in the United States. The schematized case presented herein consists of a river channel with a depth of 6 m (at the downstream end), length of 3,100 m, and a width of 1,000 m (van Rijn 1987). The discharge is 4,000 m^3/s. The flow in the channel is partially blocked by a spurdike (groyne) with a length of 400 m and a width of 100 m as shown in Fig. 14. The bed material is assumed to be sand with $d_{50}=200$ μm and $d_{10}=150$ μm, $d_{90}=300$ μm. The water temperature is set to 10°C. The fluid density is set to 1,000 kg/m^3. The bed porosity is set to 0.4. This 3D model application is based on 10 vertical layers in curvilinear mode (minimum grid size of 10 m) with MSF=200. At the inflow boundary the specific discharge is assumed to be uniformly distributed over the width ($q=4$ m^2/s). The applied horizontal mixing coefficient is 0.5 m^2/s. Both the updated TR2004 and the older TR1993 sand transport models have been used. The latter model was used with similar input data (bed roughness $k_s=0.25$ m; $d_s=140$ μm, $w_s=0.0125$ m/s) as used by van Rijn (1987). Fig. 14 shows the computed flow velocity field at initial time ($t=0$) with increased velocities (from 0.67 up to 1.7 m/s) near the tip of the dike and a large recirculation zone downstream of the dike. Fig. 15 presents the depth-integrated suspended transport rates based on the TR1993 and updated TR2004 models along two depth-averaged streamlines (see Fig. 14), showing the gradual adjustment process of the suspended sediment transport. The adjustment of the erosion process proceeds much faster than the adjustment of the deposition process. The small irregularities in Streamline A are caused by interpolation errors, as a depth-averaged streamline is used and not the

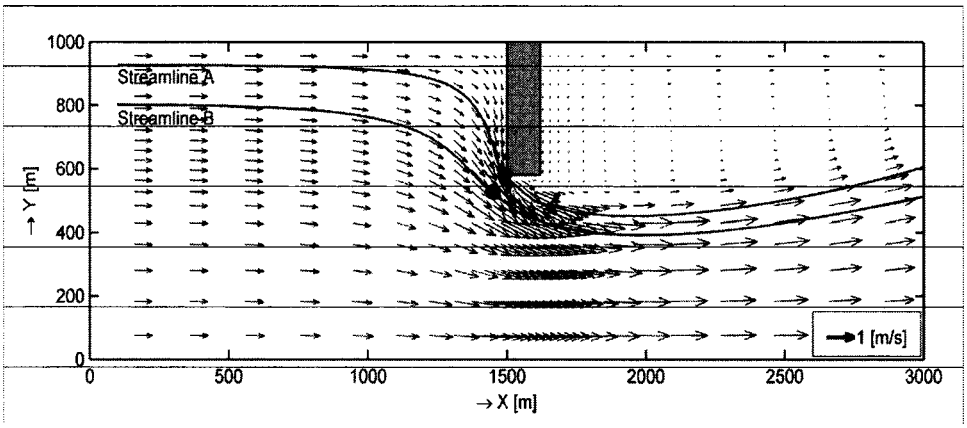

Fig. 14. Plan view of spurdike case with computed depth-averaged velocity field at initial time ($t=0$) and two depth-averaged streamlines

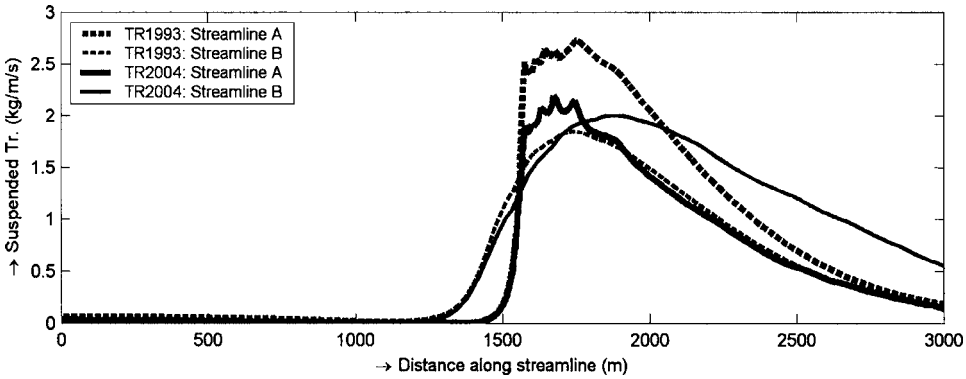

Fig. 15. Suspended transport at initial time along two streamlines based on TR2004 sand transport model and earlier TR1993 transport model

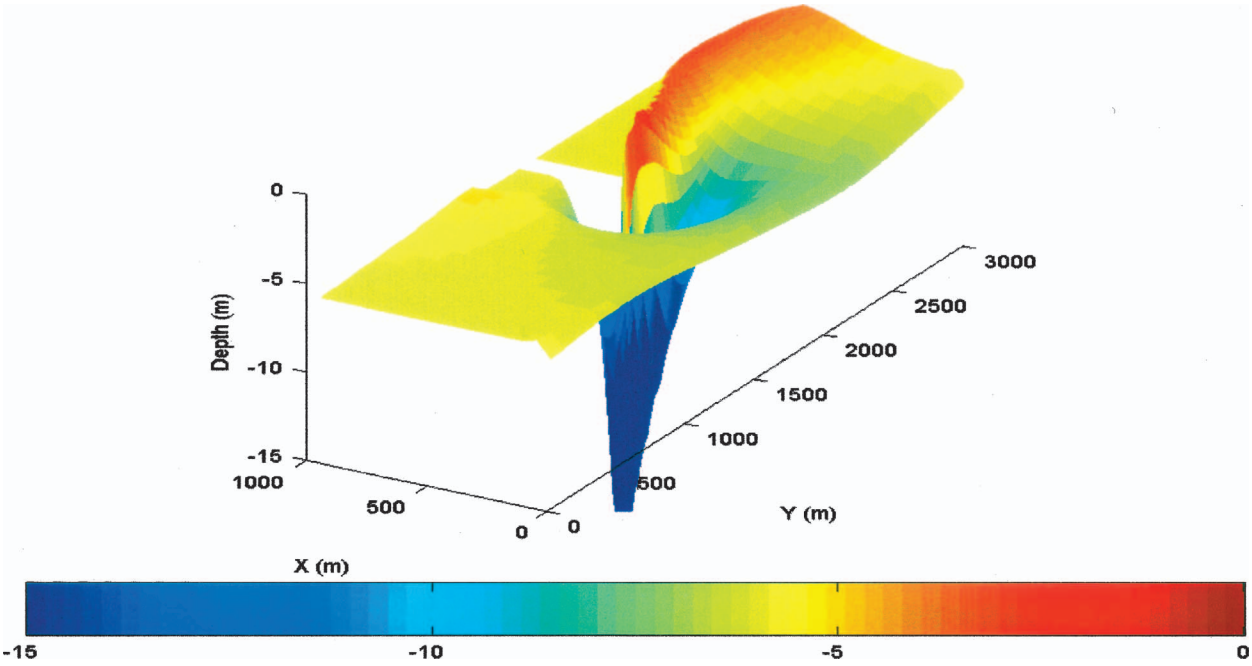

Fig. 16. (Color) 3D plot of bed evolution (in m) based on TR2000 model after 200 days with scour hole (in blue) near the tip of the dike and a deposition ridge (in red) downstream of dike; dike (in white) on left side

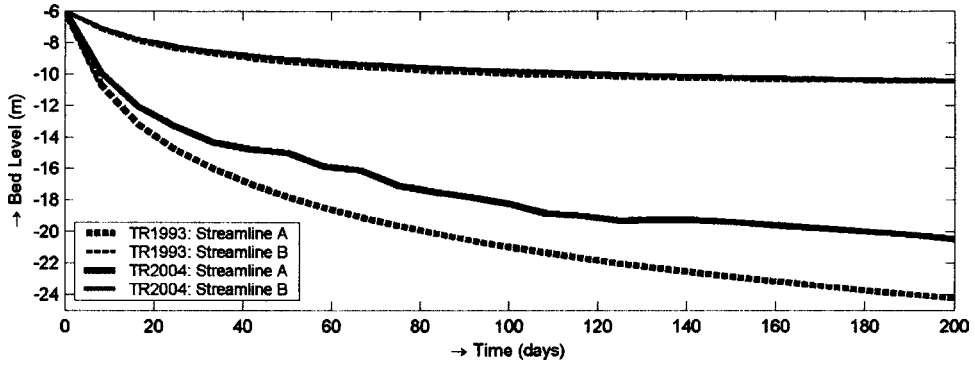

Fig. 17. Bed evolution of two stations near tip of dike in Streamlines A and B (see Fig. 14)

transport path. Fig. 16 presents the 3D bed evolution after 200 days, showing a deep scour hole (about 20 m) near the tip of the dike and a deposition ridge with a maximum height of about 3 m along the edge of the recirculation zone. Fig. 17 shows the bed evolution in time of two stations near the tip of the dike (see Fig. 14). The computed maximum scour depth near the tip of the dike is about 20 m based on the TR2004 model and about 24 m for the TR1993 model. These maximum erosion results (about 20–24 m) are in the range of 3–4 times the upstream water depth (h_o =6 m), which is in reasonable agreement with the maximum erosion depth of $3h_o$ reported by Richardson (1988) and van Rijn (2005) for the spurdike case. The time scale of the scour development was not reported; but a time period of 200 days to reach the maximum depth may be a bit short. This practical case shows that the scour depth around the tip of a structure can be rather large (many times the upstream water depth) and that measures (bed protection) should be anticipated to prevent instability of the structure.

Tidal Flow and Sediment Transport in Yangtze Estuary, China

The Yangtze River has its origin on the Tibetan plateau in the western part of China and debouches 6,300 km eastward into the Yangtze Estuary and from there into the East China Sea. The

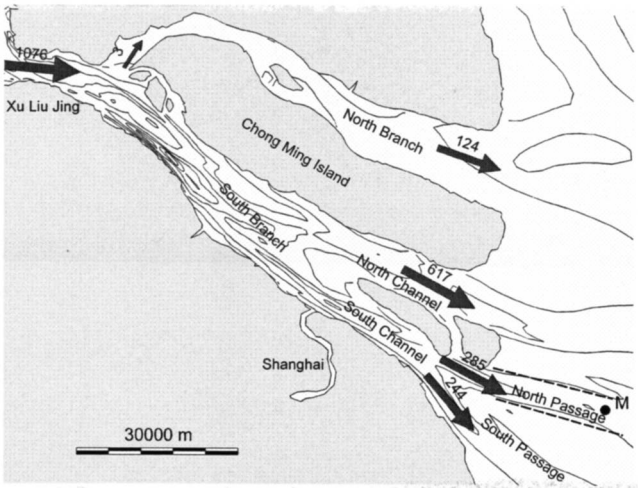

Fig. 18. Plan view of Yangtze Estuary (with sea on right side; M=monitor station in the North Passage; dashed line=training walls along North Passage); annual silt transport rates in million tons/year

daily fresh water discharge is of the order of 2.5 billion m^3 and the daily sediment discharge is of the order of 1–2 million tons (annual 500 million tons). These values roughly yield an average concentration of 0.5 kg/m^3. The Yangtze Estuary is a large-scale tidal system with a length scale of about 200 km and a width scale of about 50 km, as shown in Fig. 18. The city of Sjanghai is located on the south shore of the Yangtze Estuary. The flow of water is dominated by tide-induced (semidiurnal with maximum spring tide of about 3.5 m) and salinity-induced forces; the tidal wave propagates up to the town of Datong 600 km from the mouth. At a distance of about 150 km from the mouth (near Xu Liu Jing), the Yangtze River splits into two branches: the North Branch and the South Branch surrounding the Chong Ming Island. The South Branch is the dominant branch, through which more than 90% of the discharge of water and sediment is conveyed. At about 80 km from the mouth, the South Branch splits up into the North Channel and the South Channel separated by two islands: Chang Xin and Heng Sha. The South Channel splits again into two channels: North Passage and South Passage. The bed of the Yangtze Estuary consists of fine cohesive sediments with median particle diameters between 10 and 30 μm, which is supplied by the Yangtze River (about 500 million tons per year) (Dou et al.1999; Dou and Li 2004) and redistributed under the action of tidal currents and wind waves. The tidal velocities in the main channels are largest during ebb flow with peak velocities up to 2 m/s due to the presence of the large river discharge.

The main shipping channel from the sea is through the North Passage into the South Channel and from there either to the Port of Shanghai (via the Huang Pu River) or to the lower reaches of the Yangtze River. Since the shipping channel is limited in depth by a mouth bar with a natural depth of no more than about 6 m, intensive dredging (10–20 million m^3 per year) (Dou and Li 2004) is carried out to keep the North Passage at the required depth for navigation. The average siltation thickness in the shipping channel is of the order of 5–10 mm per day. Siltation processes are strongly affected by seawater flocculation resulting in settling velocities between 0.1 and 2 mm/s (Shi and Zhou 2004). Because the salinity in the estuary depends on the variation of the fresh water river discharge, the flocculation effects vary over the seasons (wet and dry seasons). The formation of fluid mud layers is a typical phenomenon in the North and South Passages due to flocculation resulting in relatively large settling velocities, particularly during slack tide (Li et al. 2001). These fluid mud layers can be as thick as 1 m during slack tide and are generally removed by increasing velocities during peak flow conditions. To reduce the dredging problems, the construction of a long training wall on both sides of the North Passage was started in 1998.

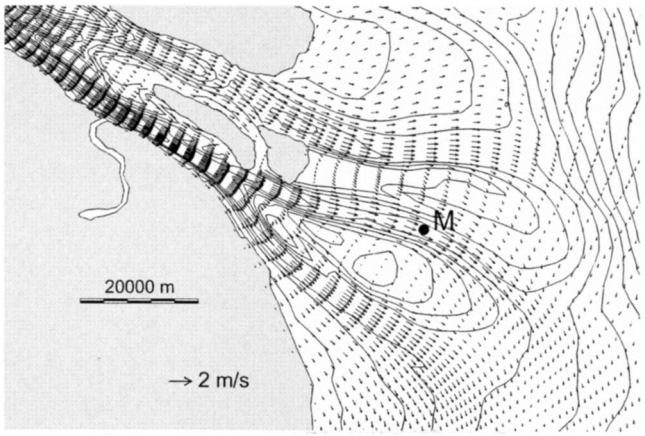

Fig. 19. Depth-averaged flow velocities (in m/s) at time of maximum ebb flow

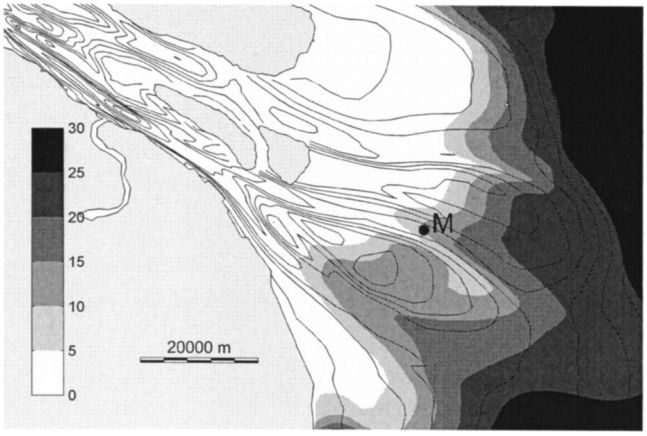

Fig. 20. Middepth salinity values (in ppt) at slack tide when salinity penetration is maximum; M=monitor station in turbidity maximum zone of the North Passage

The aim of the present study is to explore the predicting ability of the 3D model with regard to fine cohesive sediments (including salinity-induced flocculation effects) in one of the most complicated sediment environments of the world, focusing on the situation before 1998 (without training walls in the North Passage).

The model grid covers the Yangtze River up to the town of Datong (600 km from the sea). The bathymetry is based on Charts from dates prior to 1998. Chart Datum is 4.55 m below mean sea level. In all, the model grid consists of 63,000 grid points (10 grid points over the depth, 6,300 grid points in horizontal domain). The bathymetry refers to the pretraining wall situation (before 2000). The river discharge is set to an annual-average value of 28,000 m^3/s. The sea boundary conditions were derived from the larger-scale Hangzhou Bay model through a nesting procedure. A set of astronomical tidal components was derived for each section of the seaward boundary of the model. Each flow simulation was executed for a period of 8 weeks, starting at January 1 and consisting of a spin-up period of 6 weeks and 2 weeks of results for the final spring–neap cycle. The spin-up period is mainly required for the adjustment of the salinity values and hence the sediment concentration values which depend on the salinity-induced flocculation processes. At the seaward boundary, a constant salinity value of 31 ppt (promille) is used and 0 ppt at the upstream river boundary. The sediment transport model is applied with default settings which means that all effects are included (flocculation, hindered settling, turbulence damping, cohesive effects on initiation of motion, as proposed in Parts 1 and 2). The median particle size of the bed material is set to 20 μm (0.02 mm). The silt concentrations at the upstream boundary are set to a value of 2 and 0.1 kg/m^3 at the seaward boundary. The bed roughness is predicted by the model based on the sediment and hydrodynamic parameters. The flocculation effect is based on linear adjustment from zero effect to maximum effect for salinities between 0 and 1 ppt, which means that the flocculation process is assumed to fully effective when the salinity value exceeds 1 ppt. This latter threshold was also set to 10 ppt and to 100 ppt (almost no flocculation) to study the effect of flocculation on settling velocities, concentrations and net transport rates.

The flow of water in the estuary is rather complicated due to the interaction of the tidal propagation (salt water) and the river run off (fresh water). It takes about 4 h for the tidal wave to travel from the mouth up to the town of Xu Liu Jing just west of the confluence of the North and the South Branches. As the tidal wave travels up the estuary, the mean water level increases and the tidal range decreases somewhat. The maximum tidal range at Xu Liu Jing is about 3.5 m during Spring tide. The total river runoff over the spring–neap cycle of about 15 days is about 36 billion m^3. The flood volume (integrated over the spring–neap cycle of about 15 days) passing through the mouth of the North Branch is 32 billion and 60 billion m^3 through the three mouths (South passage, North passage, and North Channel) of the South Branch. The ebb volume through the mouth of the North Branch is 34 billion and 94 billion m^3 through the South Branch. This implies that only 2 billion m^3 (34–32) or about 6% of river runoff is conveyed through the North Branch and about 34 billion m^3 (94–60) or 94% of the runoff through the South Branch. Thus, only a very small portion of the fresh water is conveyed through the North Branch.

Fig. 19 presents the depth-averaged flow velocity at the time of maximum ebb flow showing values up to 1.6 m/s in the main channels. The time variation (over 3 days) of the depth-averaged flow velocity in Monitor Station M in the North Passage (see Fig. 19) is given in Fig. 21 (most left velocities are ebb flow followed by flood flow, etc.). The ebb velocities are varying weakly between 1.2 and 1.6 m/s, whereas the flood velocities show a much larger variation between 0.8 and 1.4 m/s depending on the tidal characteristics (diurnal and semidiurnal components). Fig. 20 presents the middepth salinity values at slack tide showing that the salt penetration is largest just south of the North passage and in the North Branch causing flocculation and enhanced deposition. These zones are generally known as the turbidity maximum. These salinity patterns are in excellent agreement with salinity observations presented by Shi (2004) for the North Passage. The time variation of the middepth salinity in the Monitor Station M situated in the turbidity maximum of the North Passage is presented in Fig. 21, showing maximum salinity values at the time of flow reversal from flood flow to ebb flow. The middepth salinity, typically, shows a high value of about 15 ppt and a low value of about 3 ppt at flow reversal from flood to ebb, depending on the magnitude of the actual flood velocity. These features are of crucial importance for the variation of the flocculation and settling velocities and hence for the variations of the silt concentrations shown in Fig. 21. The minimum settling velocity (shown in Fig. 22) without flocculation is about 0.35 mm/s based on the sediment size of 20 μm and the input water temperature of 15°C. This value increases to a maximum value of about 1.5 mm/s between February 20 and 21 when the salinity, and hence, the

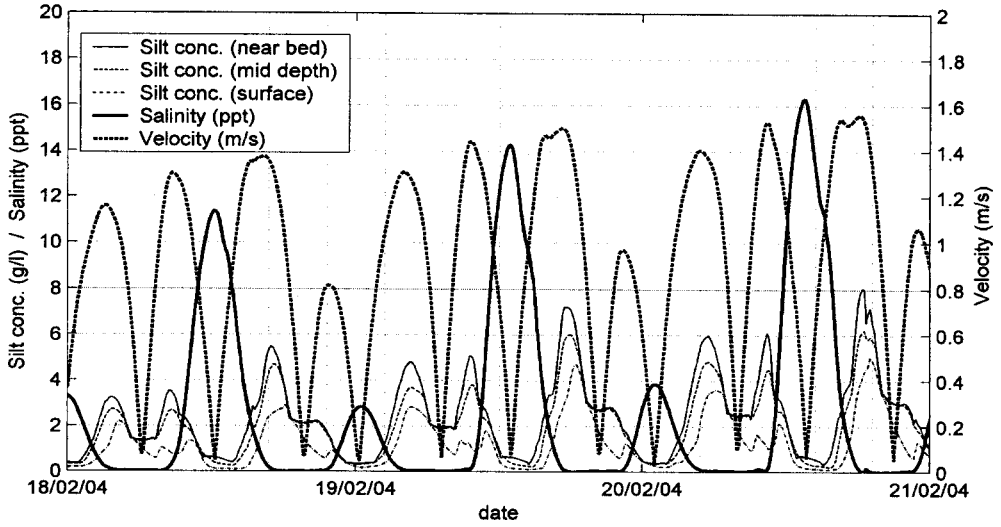

Fig. 21. Silt concentrations at three heights above bed (in g/l or kg/m^3), Middepth salinity (in ppt; scale of 0–20 ppt) and depth-averaged velocity (in m/s; most left velocity peak is ebb flow); salinity threshold for flocculation=1 ppt, Station M

flocculation is maximum (16 ppt, see Fig. 22). These settling velocity values are in good agreement with observed values of Shi and Zhou (2004). The settling velocities are largest near the bed where the concentrations are largest, shown in Fig. 21. During flood flow, the settling velocities are largest just after peak flood flow when the salinities are increasing. During ebb flow, the settling velocities are maximal just before peak ebb flow when the salinities are decreasing. The silt concentrations at peak flood and ebb flows vary between 3 and 8 kg/m^3 near the bed and between 2 and 5 kg/m^3 near the water surface. These maximum values are in excellent agreement with the measured values of 3–5 kg/m^3 in the North Passage given by Li et al. (2000). During slack tide from flood to ebb flow when the salinity is maximum (about 15 ppt) and hence flocculation is maximum and the concentrations fall back to values between 0 and 1 kg/m^3 and deposition is maximum during this period resulting in fluid mud layer formation. The time-averaged (net) silt transport rates scaled up to annual values (assuming 25 neap–spring cycles in a year) through boundaries west and east of Chong Ming Island are shown in Fig. 18, yielding a value of about 1,000 million tons per year at the west boundary. This latter value is in a very encouraging agreement with the observed value of 500 million tons per year (Shi 2004), particularly when it is realized that the model is applied using default values without any calibration of the model. Most of the deposition takes place in the North and South Passages beyond Chong Ming Island in good agreement with observations (Dou and Li 2004). A run with inclusion of the training walls along the North Passage shows that the net annual silt transport through the North Passage is reduced by about 35% (from about 290–190 million tons, see Fig. 18). The settling velocities are quite sensitive to the salinity threshold (1, 10, and 100 ppt) used in this study. However, the effect on the silt concentrations is not so large as the salinity is maximum during slack tide when the concentrations are relatively small. The concentrations are smallest for a threshold of 1 ppt (fast response of flocculation) and largest for 100 ppt (almost no flocculation). In the latter case the concentration profile is much more uniform over the depth (lower settling velocities). The gross (absolute values) sediment transport rates integrated over the tide in station M are 610, 730, and 840 tons/m for salinity threshold values of 1, 10, and 100 ppt,

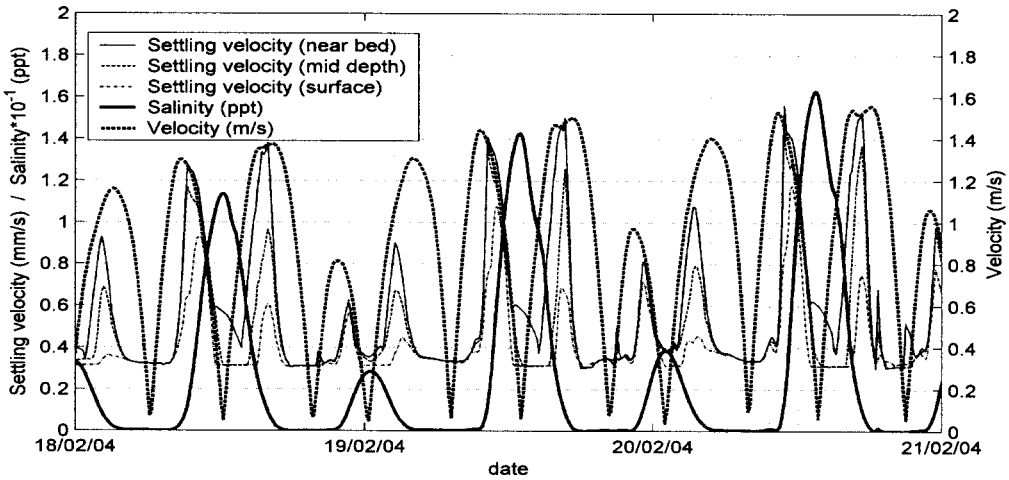

Fig. 22. Settling velocities at three heights above bed (in mm/s), middepth salinity (in ppt; scale of 0–20 ppt) and depth-averaged velocity (in m/s; most left velocity peak is ebb flow); salinity threshold for flocculation=1 ppt, Station M

respectively. Thus, about 20% smaller in the reference case with a salinity threshold of 1 ppt than for a threshold of 10 ppt and 40% smaller than for a threshold of 100 ppt (almost no flocculation). The net transport rates integrated over the tide in Station M are 210, 210, and 180 tons/m and are thus not much affected (only 10%) by the threshold salinity value.

Conclusions

The TR2004 transport formulations for clay, silt, and sand as proposed in Parts 1 and 2 have been implemented in morphodynamic models. The models have been verified using various laboratory and field data cases. Furthermore, the 3D model has been applied to two complicated sediment environments concerning the flow around a spurdike in a river and the tidal flow of cohesive sediments in the Yangtze Estuary in China. The main findings of the study are summarized, as follows:

- The bed load and suspended transport of the 3D model are in good agreement with those of the stand-alone TR2004 model (maximum errors of 50% at high velocities);
- The small-scale and short-term sedimentation processes in trenches and channels can be simulated with excellent agreement to measured values;
- The long term migration (about 15 years) of an offshore sand ridge in tidal flow with combined waves can be simulated with sufficient accuracy when a multilayer approach is used;
- The cross-shore behavior of breaker bars in the near-shore can be represented qualitatively using a 2D model approach;
- The flow and suspended transport around a long spurdike in a river generate a deep scour hole near the tip of the dike with a maximum depth of about three to four times the upstream water depth on the time scale of 1 year; and
- The flocculation processes and associated settling velocities and transport rates in the large-scale saline Yangtze Estuary in China can be simulated rather well using default values of the 3D model; the construction of a training wall along a shipping channel (North Passage) reduces the inflow of sediments considerably.

Overall, it is concluded that the morphodynamic models using default settings perform reasonably well. The applied scaling factors of the sediment transport model are in the generally-accepted range of 0.5 to 2 for all runs considered.

Acknowledgments

The National Institute for Coasts and Sea (RIKZ/Rijkswaterstaat, The Netherlands) is gratefully acknowledged for providing research funds within the Generic Coastal Research Programme (VOP), as well as the Basic Research Programme of Delft Hydraulics and the European Research Projects SEDMOC, COAST3D, and SANDPIT sponsored by the European Community Research Programme.

References

Dou, X., and Li, T. (2004). "Silt prediction of one-stage deep water channel project in the Yangtze Estuary." *Proc., 9th Int. Symp. on River Sedimentation*, Yichang, China, 1997–2002.

Dou, X., Li, T., and Dou, G. (1999). "Numerical model of total sediment transport in the Yangtze Estuary." *China Ocean Eng.*, 13(3), 277–286.

Galappatti, R. (1983). "A depth-integrated model for suspended transport." *Rep. No. 83-7*, Delft Univ. of Technology, Delft, The Netherlands.

Holthuijsen, L. H., Booij, N., and Herbers, T. H. C. (1989). "A prediction model for stationary, short-crested waves in shallow water with ambient currents." *Coastal Eng.*, 13, 23–54.

Holthuijsen, L. H., Booij, N., and Ris, R. C. (1993). "A spectral wave model for the coastal zone." *Proc., 2nd Int. Symp. on Ocean Wave Measurement and Analysis*, New Orleans, 630–641.

Lesser, G., Roelvink, J. A., Van Kester, J. A. T. M., and Stelling, G. S. (2004). "Development and validation of a three-dimensional morphological model." *Coastal Eng.*, 51, 883–915.

Li, J., He, Q., Xiang, W., Wan, X., and Shen, H. (2001). "Fluid mud transportation at water edge in the Chiangjiang Estuary." *Sci. China, Ser. B: Chem.*, 44, 47–56.

Li, J., He, Q., Zhang, L., and Shen, H. (2000). "Sediment deposition and resuspension in mouth bar area of the Yangtze Estuary." *China Ocean Eng.*, 14(3), 339–348.

Nielsen, P. (1988). "Three simple models of wave sediment transport." *Coastal Eng.*, 10, 43–62.

Nielsen, P. (1992). *Coastal bottom boundary layers and sediment transport*, World Scientific, Singapore.

Nielsen, P., and Callaghan, D. P. (2003). "Shear stress and sediment transport calculations for sheet flow under waves." *Coastal Eng.*, 47, 347–354.

Richardson, E. V. (1988). "Highways in the river environment." *Rep., Federal Highway Administration*, U.S. Dept. of Transportation, Ft. Collins, Colo.

Roelvink, J. A., Van der Kaaij, T., Ruessink, B. G. (2001). "Calibration and verification of large-scale 2D/3D flow models. Phase 1, Parcel 2, Subproduct 2." *ONL FLYLAND Rep.*, Delft Hydraulics, Delft, The Netherlands.

Sánchez-Arcilla, A., Roelvink, J. A., O'Connor, B. A., Reniers, A., and Jimenez, J. A. (1995). "The delta flume experiment." *Proc., Coastal Dynamics*, Barcelona, Spain, 488–502.

Shi, Z. (2004). "Behaviour of fine suspended sediment at the North Passage of the Chiangjiang Estuary, China." *J. Hydrol.*, 293, 180–190.

Shi, Z., and Zhou, H. J. (2004). "Controls on effective settling velocities of mud flocs in the Changjiang Estuary China." *Hydrolog. Process.*, 18, 2877–2892.

Stelling, G. S., and Van Kester, J. A. T. M. (1994). "On the approximation of horizontal gradients in sigma coordinates for bathymetry with steep bottom slopes." *Int. J. Numer. Methods Fluids*, 18, 915–955.

Sutherland, J., Peet, A. H., and Soulsby, R. L. (2004). "Evaluating the performance of morphodynamic modelling." *Coastal Eng.*, 51, 917–939.

Sutherland, J., and Soulsby, R. L. (2003). "Use of model performance statistics in modelling coastal morphodynamics." *Proc., Int. Conf. on Coastal Sediments* (CD-ROM), World Scientific, Corpus Christi, Tex.

Sutherland, J., Walstra, D. J. R., Chesher, T. J., Van Rijn, L. C., and Southgate, H. N. (2004). "Evaluation of coastal area modelling systems at an estuary mouth." *Coastal Eng.*, 51, 119–142.

Svasek, J. N. (1964). "Behaviour of trial dredge trench in the sea bed of the North Sea near Scheveningen." *Rep.*, Deltadienst, The Haque, The Netherlands (in Dutch).

Tonnon, P. K., van Rijn, L. C., and Walstra, D. J. R. (2007). "The modelling of tidal sand ridges on the shoreface." *Coastal Eng.* 54, 279–296.

Van der Werf, J. J. (2006). "Sand transport over rippled beds in oscillatory flow." Doctoral thesis, Dept. of Civil Engineering, Univ. of Twente, Enschede, The Netherlands.

van Dijk, T. A. G. P., and Kleinhans, M. G. (2005). "Processes controlling the dynamics of compound sand waves in the North Sea, The Netherlands." *J. Geophys. Res.*, 110(4), F04S10.

van Rijn, L. C. (1986). "Mathematical modeling of suspended sediment transport in nonuniform flows." *J. Hydraul. Eng.*, 112(6), 433–455.

van Rijn, L. C. (1987). "Mathematical modeling of morphological pro-

cesses in the case of suspended sediment transport." Thesis, Civil Engineering Dept., Delft Univ. of Technology, Delft, The Netherlands.
van Rijn, L. C. (1997). "Sediment transport and budget of the central coastal zone of Holland." *Coastal Eng.*, 32, 61–90.
van Rijn, L. C. (2005). *Principles of sedimentation and erosion engineering in rivers, estuaries, and coastal seas*, Aqua Publications, Blokzijl, The Netherlands.
van Rijn, L. C., and Havinga, F. (1995). "Transport on fine sands by currents and waves. Part 2." *J. Waterway, Port, Coastal, Ocean Eng.*, 121(2), 123–133.
van Rijn, L. C., Ruessink, G., and Grasmeijer, B. T. (1999). "Generation and migration of nearshore bars under non- to macrotidal conditions." *Proc., Coastal Sediments*, ASCE, Reston, Va., 463–478.
van Rijn, L. C., Soulsby, R. L., Hoekstra, P., and Davies, A. G. (2005). *Sand transport and morphology of offshore sand mining pits*, Aqua Publications, Blokzijl, The Netherlands.
van Rijn, L. C., Walstra, D. J. R., Grasmeijer, B., Sutherland, J., Pan, S., and Sierra, J. P. (2003). "The predictability of cross-shore bed evolution of sandy beaches at the time scale of storms and seasons using process-based profile models." *Coastal Eng.*, 47, 295–327.
van Rijn, L. C., Walstra, D. J. R., and Van Ormondt, M. (2004). "Description of TRANSPOR 2004 (TR2004) and implementation in DELFT3D-online." *Rep. Z3748*, Delft Hydraulics, Delft, The Netherlands.
Van Woudenberg, C. C. (1996). "Artificial sand ridge at location Hoek van Holland." *Rep. NZ-96.03*, Noordzee, The Hague, The Netherlands (in Dutch).
Walstra, D. J. R., et al. (1997). "Large-scale and long-term effects of Maasvlakte-2 and related sand mining alternatives: Morphological effects on Dutch Coast of Zeeuws-Vlaanderen to Den Helder over a period of 300 years." *Alkyon Rep.*, Delft Hydraulics, Delft, The Netherlands (in Dutch).
Walstra, D. J. R., Roelvink, J. A., and Groeneweg, J. (2000). "Calculation of wave-driven currents in a 3D mean flow model." *Proc., 27th Int. Conf. on Coastal Engineering*, Sydney, Australia, 1050–1063.
Walstra, D. J. R., van Rijn, L. C., Boers, M., and Roelvink, D. (2003). "Offshore sand pits: Verification and application of a hydrodynamic and morphodynamic model." *Proc., Coastal Sediments* (CD-ROM).
Walstra, D. J. R., van Rijn, L. C., and Klein, A. (2004). "Validation of a new transport formula (TRANSPOR2004) in a three-dimensional morphological model." *Proc., 29th Int. Conf. on Coastal Engineering*, Lisbon, Portugal, 2703–2715.
Wang, S. S. Y., and Wu, W. (2005). "Computational simulation of river sedimentation and morphology: A review of the state of the art." *Int. J. Sediment Res.*, 20(1), 7–29.